# High Drag States in Tidally Modulated Stratified Wakes

PRANAV PUTHAN,[a] GENO PAWLAK,[a,b] AND SUTANU SARKAR[a,b]

[a] *Department of Mechanical and Aerospace Engineering, University of California, San Diego, La Jolla, California*
[b] *Scripps Institution of Oceanography, University of California, San Diego, La Jolla, California*

ABSTRACT: Large-eddy simulations (LES) are employed to investigate the role of time-varying currents on the form drag and vortex dynamics of submerged 3D topography in a stratified rotating environment. The current is of the form $U_c + U_t \sin(2\pi f_t t)$, where $U_c$ is the mean, $U_t$ is the tidal component, and $f_t$ is its frequency. A conical obstacle is considered in the regime of low Froude number. When tides are absent, eddies are shed at the natural shedding frequency $f_{s,c}$. The relative frequency $f^* = f_{s,c}/f_t$ is varied in a parametric study, which reveals states of high time-averaged form drag coefficient. There is a twofold amplification of the form drag coefficient relative to the no-tide ($U_t = 0$) case when $f^*$ lies between 0.5 and 1. The spatial organization of the near-wake vortices in the high drag states is different from a Kármán vortex street. For instance, the vortex shedding from the obstacle is symmetric when $f^* = 5/12$ and strongly asymmetric when $f^* = 5/6$. The increase in form drag with increasing $f^*$ stems from bottom intensification of the pressure in the obstacle lee which we link to changes in flow separation and near-wake vortices.

KEYWORDS: Topographic effects; Eddies; Tides; Vortices; Large eddy simulations; Nonhydrostatic models

## 1. Introduction

Rough bottom topography in the abyssal ocean contributes significantly to enhancement of drag and turbulent dissipation. When abyssal flow encounters rough topography, energy is lost in two ways: 1) skin friction resulting from tangential stress at the boundary and 2) via pressure/form drag resulting from normal stress. Recent studies of Zhang and Nikurashin (2020) and Klymak (2018) highlight the crucial role played by multiscale topography in extracting momentum (through topographic form stress) from the background flow and maintaining a dynamic balance in the abyssal ocean. Form drag is often the primary mechanism of energy extraction from the barotropic tide, especially at steeper topographies (McCabe et al. 2006; Horwitz et al. 2021).

In situ measurements show that the loss of momentum associated with form drag is enhanced by obstacles including coastal headlands (Edwards et al. 2004; Magaldi et al. 2008; Warner et al. 2012; Warner and MacCready 2014) and continental shelf banks (Nash and Moum 2001; Wijesekera et al. 2014). However, observational studies of form drag estimates from the abyssal ocean are limited. Lack of information on the magnitude and spatial distribution of form drag presents a challenge for form drag parameterizations in global climate models (GCMs). Numerical studies can play an important

role in bridging this gap. Warner and MacCready (2009) performed numerical simulations with the hydrostatic ROMS model of a nonrotating tidal flow past a Gaussian headland to examine different components of form drag. They showed that while the normalized separation drag (the average drag coefficient) increased with an increase in the aspect ratio of the headland, it does not depend on the tidal excursion or the headland size. While these results may explain the momentum loss at regions where the tidal constituents dominate (e.g., Clément et al. 2017), the behavior in regions where a strong mean flow occurs in conjunction with tidal oscillations remains to be explored. In the present work, we examine form drag in tidally modulated flow past an underwater obstacle. Turbulence resolving simulations enable us to study the time varying flow past obstacles without compromising on the accuracy of their representation. The characterization of flow separation and pressure distribution on the obstacle allows us to link underlying physical mechanisms to changes in the observed form drag.

Form drag on an obstacle is dependent on the ambient stratification. When a steady current encounters a 3D ridge, the flow transitions to a state of high drag when the Froude number reduces below 1 (e.g., Epifanio and Durran 2001; Vosper et al. 1999). In situ tidal measurements of form drag are challenging and there are few such observations, e.g., Voet et al. (2020), who infer pressure from density measurements using the hydrostatic approximation. Additionally, tide induced unsteadiness may lead to changes in flow separation and distribution of lee vorticity. For example, tidal currents create transient lee eddies (or lee vortices) in wakes behind headlands (Pawlak et al. 2003; Callendar et al. 2011; MacKinnon et al. 2019) and submerged topography (Girton et al. 2019). Complexity in the impinging flow, variable stratification and irregular bathymetry at these sites present a challenge in elucidating the role of lee eddies. To examine the role of tides in

flow separation and form drag, we perform turbulence-resolving simulations of an oceanic wake past a conical hill generated by a tidally modulated flow. The background flow may be expressed as $U_b = U_c + U_t \sin(\Omega_t t)$, where $U_c$ and $U_t$ are the mean and tidal components and $\Omega_t = 2\pi f_t$ is the tidal frequency (in rad s$^{-1}$).

Stratification, rotation, and tidal forcing are key elements of geophysical wakes. When a tidally modulated flow encounters an underwater obstacle, the wake structure is governed predominantly by the obstacle Froude number (Fr$_c$), the tidal excursion number (Ex$_t$), the Rossby number (Ro$_c$), and velocity ratio ($R$):

$$\mathrm{Fr}_c = \frac{U_c}{Nh}; \mathrm{Ex}_t = \frac{U_t}{\Omega_t D}; \mathrm{Ro}_c = \frac{U_c}{fD}; R = \frac{U_t}{U_c},$$

where $N$ is the background buoyancy frequency, $f$ is the inertial frequency, $h$ is the height of the obstacle, and $D$ is the obstacle base diameter. In unstratified environments, a hill with a 3D geometry does not shed vortices similar to the vertically coherent lee eddies which are observed in the ocean. Instead a standing horseshoe vortex and periodic hairpin vortices are observed downstream at low Reynolds number (Re$_D$) (see Acarlar and Smith 1987), which become indistinct at higher Reynolds number (Garcia-Villalba et al. 2009). A low Fr$_c$ (Fr$_c \ll 1$) flow is constrained to move around rather than over the obstacle, owing to the large potential energy barrier. This leads to roll-up of the lateral shear layer into lee vortices (Hunt and Snyder 1980).

Topographic wakes are also affected by planetary rotation. A relatively large planetary rotation rate (small Ro$_c$) induces asymmetry in the strength of cyclonic and anticyclonic eddies shed from the topography (Dietrich et al. 1996). Dong et al. (2006) attributed the loss in symmetry to centrifugal instabilities in the wake. Perfect et al. (2018) and Srinivasan et al. (2018) showed that the change in vertical structure of wake vortices is governed by the Burger number Bu, defined as (Ro$_c$/Fr$_c$)$^2$. Their idealized simulations show decoupling of vortices along their vertical extent owing to loss of geostrophic balance, when Bu > 12. Recently, Jagannathan et al. (2021) and Srinivasan et al. (2021) investigated the generation mechanisms and spatial organization of lee vorticity in topographic wakes. Other outcomes of flow–topography interactions such as generation of lee waves, upstream blocking, and hydraulic jumps have also received attention in literature (e.g., Epifanio and Rotunno 2005; Wright et al. 2014; Jagannathan et al. 2019; Perfect et al. 2020).

The regime of weak rotation and strong stratification (or equivalently, large Bu) applies to wakes behind abyssal hills. For example, consider the abyssal hills in the Brazil Basin (Ledwell et al. 2000; Nikurashin and Legg 2011). The bottom topographic roughness is $O(1)$ km in the horizontal. For an obstacle with $D = 1.5$ km, buoyancy period of 1 h and $U_c = U_t = 10$ cm s$^{-1}$, the tidal excursion number is Ex$_t \approx 0.5$ for the M$_2$ tide and the average value of Fr$_c$ lies close to 0.2. The value of Rossby number is Ro$_c \approx 3$, at 15°S latitude. The resolution of GCMs is insufficient to resolve these hills. Thus,

parameterization of the wake dynamics at these length scales is critical.

Owing to numerical constraints, idealized simulations often ignore tidal forcing. Yet, in situ observations affirm that tides can significantly influence flow separation at islands, continental slopes, and submerged topography. Observations by Black and Gay (1987) showed the formation of "phase" eddies in the continental shelf of Great Barrier Reef. Denniss et al. (1995) and Chang et al. (2019) reported lee eddies shed past islands at the dominant tidal frequency. This phase-locking phenomenon is observed even when the tidal velocity amplitude is not large relative to the mean flow.

Recently Puthan et al. (2021) found tidal synchronization in a study of flow past a conical hill where the frequency of the far-wake lee vortices locked to a subharmonic (depending on the value of $f^* = f_{s,c}/f_t$) of the tidal frequency. The relative frequency ($f^*$) is linearly related to Ex$_t$ as $f^* = 2\pi \mathrm{St}_c \mathrm{Ex}_t/R$, where St$_c$ is the vortex shedding Strouhal number in a steady background flow. This relation simplifies to $f^* = 1.66\mathrm{Ex}_t$ for the hill wake (St$_c = 0.265$) when $R = 1$. However, the near wake characteristics such as flow separation at the hill and the attendant form stress were not studied by Puthan et al. (2021) and have not received adequate attention in other previous studies. Moreover, the effect of tidal modulations on flow separation is often ignored in literature (e.g., Puthan et al. 2020).

In this work, we address the questions pertaining to momentum loss of tidally modulated abyssal currents during flow–topography interactions at the obstacle and the associated wake-vorticity distribution. The motivation for this work is twofold. We explore possible states of large form drag owing to changes in pressure distribution in the lee and determine the qualitative changes to the vorticity distribution in the near wake in each state. The numerical formulation is detailed in section 2. Section 3 introduces the parameter space and lists the cases performed in the study. A brief introduction to form stress and an overview of previous literature related to form drag is provided in section 4. Section 5 elucidates the changes in form drag on varying $f^*$ and section 6 elucidates the underlying changes to flow separation. The paper concludes with discussion and conclusions in section 7.

## 2. Computational model

The computational domain is 9.5 km in the streamwise ($x$) direction, 3.8 km in the spanwise ($y$), and 2 km in the vertical ($z$) direction. The conical obstacle of height $h$ and base diameter $D$ is placed at the origin. For convenience, the horizontal and vertical distances are normalized by $D$ and $h$ such that $x^* = x/D$, $y^* = y/D$, and $z^* = z/h$. The problem setup is illustrated in Fig. 1. A barotropic unidirectional current $U_b = U_c + U_t \sin(2\pi f_t t)$ encounters a conical obstacle in a uniformly stratified environment.

The 3D nonhydrostatic flow is modeled by the Navier–Stokes equations under the Boussinesq approximation. The equations for conservation of mass, momentum and density on an $f$ plane are given below in tensor notation:

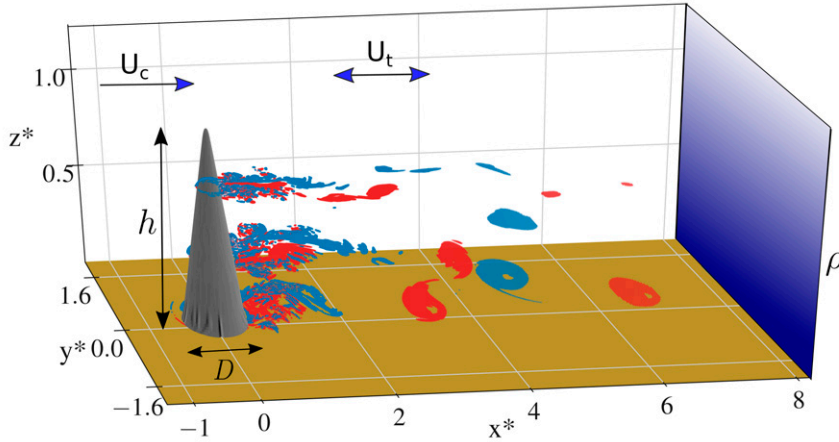$$\frac{\partial u_m}{\partial x_m} = 0, \tag{1}$$

FIG. 1. The numerical model setup is shown for the following model problem: a tidally modulated current encounters a conical obstacle in a stratified environment. The vortex shedding pattern in three horizontal planes for case $f^* = 2/15$ is represented using isosurfaces of vertical vorticity corresponding to $\omega_z/f = \pm 10$.

$$\frac{\partial u_m}{\partial t} + \frac{\partial(u_n u_m)}{\partial x_n} - f\epsilon_{mn3}(u_n - U_b \delta_{n1})$$

$$= -\frac{1}{\rho_0}\frac{\partial p}{\partial x_m} - \frac{g\rho'}{\rho_0}\,\delta_{m3} + \frac{\partial\tau_{mn}}{\partial x_n}, \tag{2}$$

$$\frac{\partial\rho}{\partial t} + \frac{\partial(u_n\rho)}{\partial x_n} = \frac{\partial\Lambda_n}{\partial x_n}. \tag{3}$$

where, $u_m = (u_1, u_2, u_3) = (u, v, w)$ denotes the velocity components and $\rho$ is the density field. Here, $\rho'$ represents deviation of density from its background value and $p$ is the deviation from the mean pressure imposed by geostrophic and hydrostatic balance. The pressure deviation $p$ may be represented as

$$p = p_d + (x - x_0)\frac{\partial p_\infty}{\partial x}, \tag{4}$$

where $\partial p_\infty/\partial x = -\rho_0 dU_b/dt = -\rho_0 U_t \Omega_t \cos(\Omega_t t)$ is the pressure gradient driving the barotropic current $U_b$ and $p_d$ is the dynamic pressure. The stress tensor $\tau_{mn}$ and density flux vector $\Lambda_n$ are computed using the approach of Puthan et al. (2020). The grid parameters, time-advancement scheme and boundary conditions are adopted from Puthan et al. (2021).

## 3. Simulation parameters

A regime of weak rotation and strong stratification is considered in the study. Inertial effects on the wake are weak in the lee of abyssal hills and headlands at length scales of $O(1)$ km at low latitudes (Rudnick et al. 2019; Liu and Chang 2018). These flows may be classified under the high Rossby number regime ($Ro_c > 1$). The inertial frequency is set to its value at 15°N such that $Ro_c = 5.5$. Much of the topography in the abyssal ocean is subject to flow conditions with $Fr_c \ll 1$,

e.g., Nikurashin and Ferrari (2010). To this end, we consider a topographic Froude number $Fr_c$ of 0.15 where the flow is predominantly around the obstacle, creating coherent vortices as observed in geophysical wakes (Perfect et al. 2018).

Tidal modulations are added to the mean flow. We consider tidal velocities of amplitude equal to the mean current, so that $R = U_t/U_c = 1$. The relative frequency $f^* = f_{s,c}/f_t$ is varied from 0.1 to 1 in a parametric study with nine cases to examine the variations in vortex dynamics and form drag. Since $f^* = 2\pi St_c Ex_t/R = 1.66 Ex_t$, this parameter space governs flows with $Ex_t$ varying from 0.06 to 0.6 (assuming $St_c = 0.265$), values of relevance in the ocean (Signell and Geyer 1991; Edwards et al. 2004; Musgrave et al. 2016). Therefore, $f^*$ is proportional to the ratio of the tidal excursion distance $U_t/f_t$ to the obstacle diameter $D$. At a constant tidal frequency $f_t$, e.g., the $M_2$ tide, larger values of the nondimensional parameter $f^*$ are associated with obstacles of smaller length scales. It is more convenient to change $f^*$ by changing the tidal frequency $f_t$ in the numerical setup. Therefore, in this parametric study, we modify $f_t$ to explore the influence of varying $f^*$.

Different regimes of tidal synchronization were observed by Puthan et al. (2021), wherein the lee vortices in the far wake were found at frequencies $f_{s,c}$, $f_t/4$, or $f_t/2$. These regimes are listed in Table 1. Regime 1 consists of a single case ($f^* = \infty$) with no tidal modulations in the background flow (i.e., $R = 0$). In regimes 2–4, $R$ equals 1 and multiple cases are explored within each regime at discrete $f^*$ values. As listed in the second column of Table 1, one case is chosen to illustrate each regime: $f^* = 2/15, 5/12$, and $5/6$ cases, for regimes 2, 3, and 4, respectively. Each regime has a distinctive near-wake vortex shedding pattern (listed in the fifth column of Table 1). The differences in the vortex shedding at the hill play a crucial role in changing the topographic pressure distribution, motivating our study of the role of $f^*$ on the separation of vortices at the obstacle and its influence on form drag.

TABLE 1. Different cases in this study: the relative frequency $f^* = f_{s,c}/f_t$ is varied among nine cases. Four regimes with different patterns of wake vortices are observed and are discussed with representative cases shown in the table. The values of $Re_D$, $Fr_c$, and $Ro_c$ are fixed at 20 000, 0.15, and 5.5, respectively.

| Regime | Case | Category | Far wake shedding frequency ($f_s$) | Near wake vortex shedding pattern |
|--------|------|----------|-------------------------------------|-----------------------------------|
| 1 | $f^* = \infty$ | No tides | $f_{s,c}$ | Kármán vortex street |
| 2 | $f^* = 2/15$ | $f^* < 1/4$ | $f_{s,c}$ | Vortex pulses + Kármán vortex street |
| 3 | $f^* = 5/12$ | $1/4 \leq f^* < 1/2$ | $f_t/4$ | Symmetric twin dipoles |
| 4 | $f^* = 5/6$ | $1/2 \leq f^* \leq 1$ | $f_t/2$ | Strong asymmetric shedding |

## 4. Form drag in oscillatory flows

Flow–bathymetry interactions result in pressure differences across abyssal obstacles, which manifests as form drag. Recent measurements at Palau estimated large form drag acting on the tidal and mean components of the flow at very low Froude numbers (Voet et al. 2020). The drag force due to form drag is computed as

$$F_D = -\int p \delta_{1j} n_j dA \cdot$$  (5)

Using Eq. (4), Eq. (5) may be expanded as

$$F_D = -\int p_d \delta_{1j} n_j dA + \rho_0 \mathcal{V} \frac{dU_b}{dt} \cdot$$  (6)

The first term on the right-hand side of Eq. (6) includes contributions from two sources: (i) the separation drag associated with flow separation at the obstacle ($F_D^S$) and (ii) the added mass ($F_D^A$) (Lamb 1930; Keulegan and Carpenter 1958). The drag associated with added mass is approximated in literature (e.g., Morison et al. 1950) using the relation

$$F_D^A = C_a \rho_0 \frac{dU_b}{dt} \mathcal{V},$$  (7)

where $C_a$ is the added mass coefficient. The second term on the right-hand side of Eq. (6) represents the Froude–Krylov force ($F_D^{FK}$) associated with the oscillating pressure gradient $p_\infty$ (Yu et al. 2018). The sum of the added mass force ($F_D^A$) and the Froude–Krylov force ($F_D^{FK}$) is referred to as inertial drag ($F_D^I$):

$$F_D^I = F_D^{FK} + F_D^A = \rho_0 \frac{dU_b}{dt} \mathcal{V} + C_a \rho_0 \frac{dU_b}{dt} \mathcal{V} \cdot$$  (8)

Therefore, the total drag force in Eq. (6) can now be written as (e.g., Warner and MacCready 2009)

$$F_D = F_D^S + F_D^A + F_D^{FK} = F_D^S + F_D^I.$$  (9)

Warner and MacCready (2009) concluded that the net contribution of inertial drag vanishes when averaged over a tidal cycle. Therefore, its contribution is estimated using Eq. (8), and removed from $F_D$ [computed using Eq. (6)] to compute the separation drag. The separation drag is assumed to be in phase with $U_b$ while the inertial drag variability has a phase difference of $\pi/2$ with respect to $U_b$ (Morison et al. 1950).

A similar drag force decomposition was proposed by Lighthill (1986), wherein the inviscid inertial drag is estimated from potential flow theory. However, the force decomposition of Lighthill (1986) has limitations. Sarpkaya (2001) argued that the force decomposition of Lighthill (1986) excludes the effects of viscosity on the added mass. His results also demonstrate that the added mass coefficient $C_a$ is time dependent. He asserted that the subtraction of the ideal inertial force (calculated from potential flow approximation) from the total form drag, leaves behind a force that consists of both the separation drag and an "acceleration-dependent" inertial force. However, the contribution from inertial drag is negligible in the time-averaged value of $F_D$, when the average is computed over a large time duration (spanning multiple tidal cycles) in a statistically stationary flow (Sarpkaya 2001). Thus the approximations of Warner and MacCready (2009) can serve as a theoretical basis to aid the interpretation of the present results by providing an adequate estimate of the separation drag. In other words, the time-mean of the form drag is representative of the separation drag $F_D^S$. The root-mean-square (RMS) form drag gives the magnitude of the fluctuating part of form drag. The phase-averaged form drag shows the variability of $F_D$ relative to the tidal phase. These diagnostic tools, which will be utilized in section 5, are also useful for comparing the energy loss associated with form drag across the regimes.

Observations of Edwards et al. (2004), Warner et al. (2012), and Voet et al. (2020) show that obstacles in the ocean extract energy from the mean and tidal components of the background flow. The rate of work done by form drag ($W_D$) is estimated as $F_D U_b$. Its time average, $\langle F_D U_b \rangle$, is representative of the average kinetic energy of the flow lost to form drag over a tidal cycle including local dissipation and internal wave energy flux (Egbert and Ray 2000). The rate of energy loss associated with the *mean* form drag is computed as $\langle F_D \rangle \langle U_b \rangle = \langle F_D \rangle U_c$. This includes energy loss due to flow separation and eddies. Since $F_D$ and $U_b$ are often time varying, the mean tidal energy loss $\langle F_D U_b \rangle$ is not the same as the energy loss rate driven by the time-averaged form drag $\langle F_D \rangle U_c$.

In the next section, we examine the time-averaged mean, phase averaged, and RMS values of $F_D$ defined below:

$$\text{Mean drag}: \langle F_D \rangle = \frac{\int_0^{nT} F_D dt}{nT},$$

$$\text{Phase averaged drag}: \langle F_D \rangle_\phi = \frac{\sum_{k=0}^{n} F_D(\Omega_t T k + \phi)}{n},$$

$$\text{RMS drag}: \langle F_D \rangle_{\text{rms}} = \sqrt{\frac{\int_0^{nT} (F_D - \langle F_D \rangle)^2 dt}{nT}}.$$

Here, $T$ is the tidal period, $\phi = \Omega_t t$ is the tidal phase and $n$ is the number of tidal cycles. The value of $n$ is larger than 6 for all cases. These diagnostic parameters are then employed to explain the variability of $\langle F_D U_b \rangle$ and $\langle F_D \rangle U_c$ across the cases.

## 5. Pressure anomalies in the wake

In a low $Fr_c$ environment, the encounter of a steady current with a 3D obstacle forces a significant volume of fluid to navigate laterally. This laterally driven flow separates, and wake eddies are formed in the lee. The form stress increases as a result. To examine the origin of form stress, a thorough characterization of the dynamic pressure $p_d$ is crucial. The form drag is computed as the sum of the surface integral of $p_d$ and the Froude–Krylov force, as shown in Eq. (6). Note that the surface integral of $p_d$ is inclusive of the added-mass component of inertial drag. In section 5a, the dynamic pressure field is examined in the wake and on the obstacle. Changes in eddy shedding and form stress are illustrated and quantified over the flow regimes listed in Table 1. Estimates of $F_D$ and their values relative to $f^* = \infty$ (no-tide) case, are provided in section 5b. The rate of work done by $F_D$ and its relative magnitude with respect to frictional drag are discussed in sections 5c and 5d, respectively.

### a. Mean pressure distribution

Figures 2a, 2c, 2e, and 2g show qualitative differences in the vortex shedding patterns among the cases $f^* = \infty$, 2/15, 5/12, and 5/6. On the right (Figs. 2b,d,f,h) the contours of mean dynamic pressure field are plotted. For $f^* = \infty$, shear layers elongate and separate from each side, rolling up into two attached vortices of opposite sign in the lee. With time, the attached eddies start to oscillate and eventually break off alternately to form the vortex street in Fig. 2a. The eddy which remains attached briefly, possesses a low pressure core which decays radially outward from the vortex center (not shown). The near-wake vertical vorticity values are as large as $20f$, which is in agreement with observations of high $Ro_c$ wakes (Chang et al. 2019; MacKinnon et al. 2019).

When $f^* = 2/15$, the lateral elongated shear layers are absent (Fig. 2c). Instead, at this instant, the anticyclonic (negative $\omega_z$) vortex remains attached to the obstacle as the cyclonic (positive $\omega_z$) vortex moves into the wake (see VortXY_JPO_fstar_2_15.mov in the online supplemental material). The anticyclonic vortex grows in size from repeated small pulses of vorticity (green box) created every tidal cycle. These pulses form on the lateral sides of the obstacle at the location of flow separation. The attached vortex is shed at a slower frequency of $f_{s,c}$ (Puthan et al. 2021). Since $f_t \approx 7.5 f_{s,c}$, the eddy remains attached while its circulation increases as the small pulses coalesce over 7.5 tidal cycles. Beyond $x^* = 1$, the staggered arrangement of vortices resembles a Kármán vortex street. The magnitude of mean dynamic pressure $\langle p_d \rangle$ is similar between the $f^* = \infty$ and 2/15 cases (Figs. 2b,d). A key difference with respect to the $f^* = \infty$ case is the presence of low pressure regions on the lateral sides of the obstacle in $f^* = 2/15$ (Fig. 2d), created by these vortex pulses.

The organization of vertical vorticity ($\omega_z$) and mean pressure ($\langle p_d \rangle$) for $f^* = 5/12$ and 5/6 are strikingly different from a Kármán vortex street generated by a steady current. At $f^* = 5/12$, a symmetric arrangement of vortices is present in the near wake, attached to the obstacle (Fig. 2e). However, this configuration is not stable and gives way to a distorted antisymmetric pattern of vortex fragments farther downstream. The timing of symmetric twin vortices is phase locked to the barotropic flow, elucidated further in section 5b.

Figure 2g provides a snapshot of the wake when $f^* = 5/6$. The cyclonic vortex remains attached to the obstacle lee at this instant and grows in size during the tidal acceleration phase. Contours of mean pressure reveal regions of large pressure drop in the lee for the $f^* = 5/12$ and 5/6 cases (Figs. 2f,h). For $f^* = 5/12$, two laterally offset low pressure zones lie symmetrically with respect to $y^* = 0$ while for $f^* = 5/6$, the low pressure region extends to cover the entire rear of the obstacle ($x^* > 0$). To discern the pressure anomalies along the vertical extent of the obstacle, the distribution of mean pressure field $\langle p_d \rangle$ on the hill is plotted in Fig. 3.

Figures 3a, 3d, 3g and 3b, 3e, 3h show the pressure distribution on the upstream and downstream faces of the obstacle, respectively. Each row in Fig. 3 corresponds to a different case. The panels of Figs. 3c, 3f, and 3i contrast the difference between the upstream and downstream pressure values ($\Delta \langle p_d \rangle$) integrated along $y^*$ among the three cases. The distribution of pressure on the upstream face is similar in all three tidally modulated cases. However, the differences in flow separation change the pressure distribution on the downstream face. The eddy shed from the obstacle has a larger horizontal length scale at the boundary as $f^*$ increases. This forced eddy is characterized by the presence of a low pressure core.

In all cases, $\Delta \langle p_d \rangle$ is bottom intensified. In their steady-current simulations, MacCready and Pawlak (2001) noted "a tendency for drag on the lower half of the ridge to be greater than that on the upper half." In the present tidally modulated cases, the bottom intensification progressively increases from $f^* = 2/15$ to 5/6. For example, consider the laterally integrated mean pressure at height $z^* = 0.2$ (Figs. 3c,f,i). Its value increases from 0.6 at $f^* = 2/15$ to 1 at $f^* = 5/12$. For the $f^* = 5/6$ case (Figs. 3h,i), the near-bottom integrated $\Delta \langle p_d \rangle$ is up to 5 times larger than its value at $z^* = 0.5$. A similar bottom-intensified pressure difference is also observed for $f^* = 5/12$, though for this case it is confined to the lateral sides of the abyssal hill (Figs. 3e,f). Even for $f^* = 2/15$ (Figs. 3b,c), a two-fold increase in pressure drop is observed near the bottom relative to the upper half of the obstacle.

The eddy shedding (Fig. 2) and pressure anomalies (Fig. 3) in the $f^* = 2/15$, 5/12, and 5/6 cases are characteristic of the regimes 2, 3, and 4 that they represent. An examination of the pressure variability within a tidal cycle is the next step toward revealing the underlying mechanisms governing enhancement of drag at the obstacle base.

Figure 4 shows snapshots of instantaneous normalized pressure $p_d / \rho_0 U_c^2$ in the horizontal plane $z^* = 0.02$ (close to the bottom boundary) for $f^* = 2/15$, 5/12, and 5/6 cases. Four time instants $T_1$, $T_2$, $T_3$, and $T_4$ are chosen at tidal phases $\Omega_t t = 0$, $\pi/2$, $\pi$, and $3\pi/2$, respectively, for the snapshots.
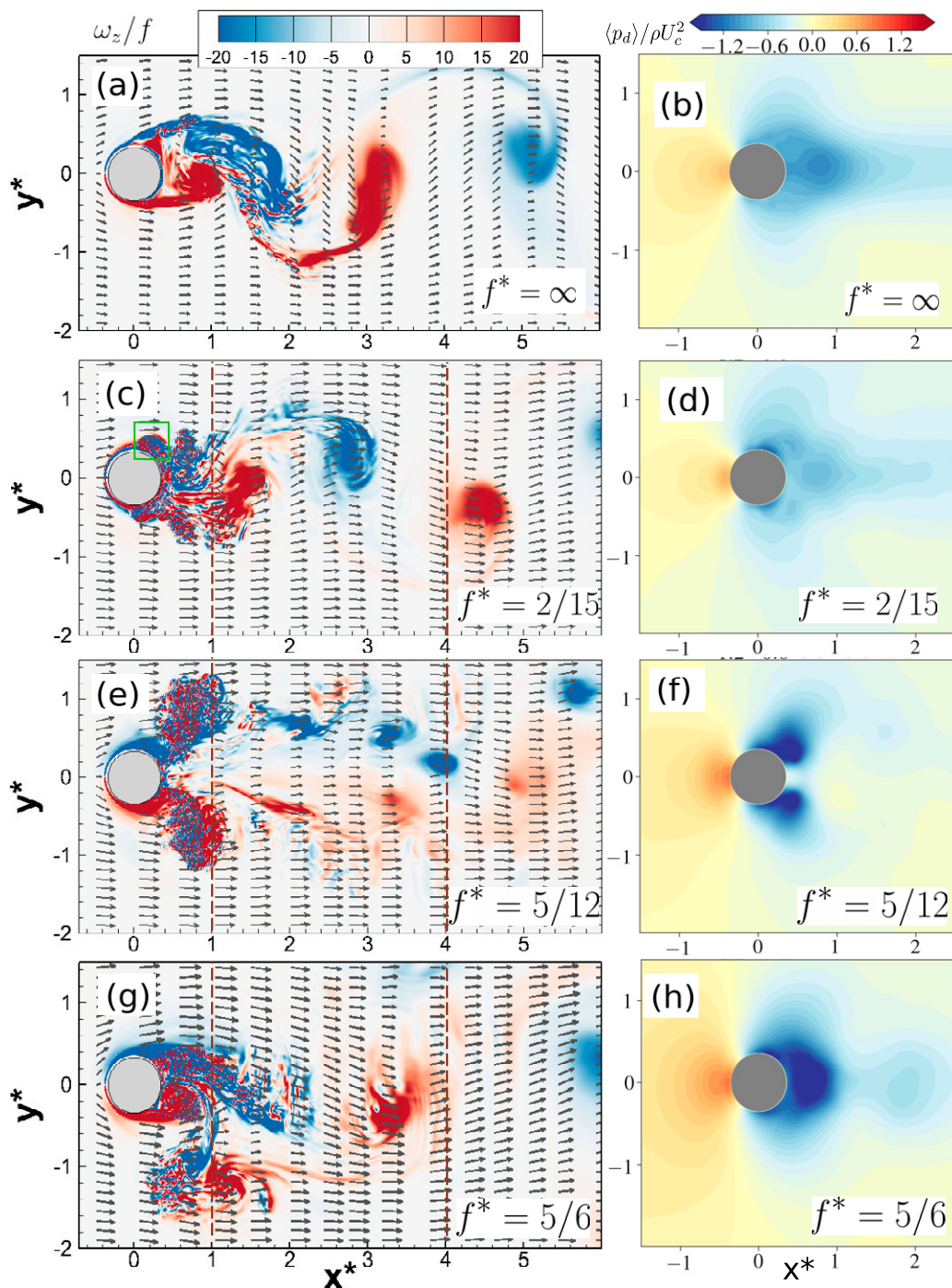
FIG. 2. Instantaneous contours of normalized vertical vorticity ($\omega_z/f$) and time-averaged pressure ($\langle p_d \rangle / \rho_0 U_c^2$) in the horizontal plane $z^* = 0.25$: (a),(b) $f^* = \infty$; (c),(d) $f^* = 2/15$; (e),(f) $f^* = 5/12$; and (g),(h) $f^* = 5/6$. In the tidally modulated cases, the contours of vorticity are plotted at the maximum velocity phase ($\Omega_t t = \pi/2$).

The variation of the phase-averaged form drag $\langle F_D \rangle_\phi$ and the barotropic current $U_b$ are plotted in the header.

Consider the case $f^* = 5/6$ (from regime 4). At $t = T_1$, the accelerating fluid impinges on the obstacle, creating high pressure upstream and a low pressure zone downstream (Fig. 4i). The

Owing to the asymmetry in flow separation, the low pressure region is dominant between $y^* = -0.5$ and 0. As the barotropic velocity increases, the region of low pressure enlarges downstream in Fig. 4j, associated with the lee eddy formation illustrated in Fig. 2g. The simultaneous increase in upstream
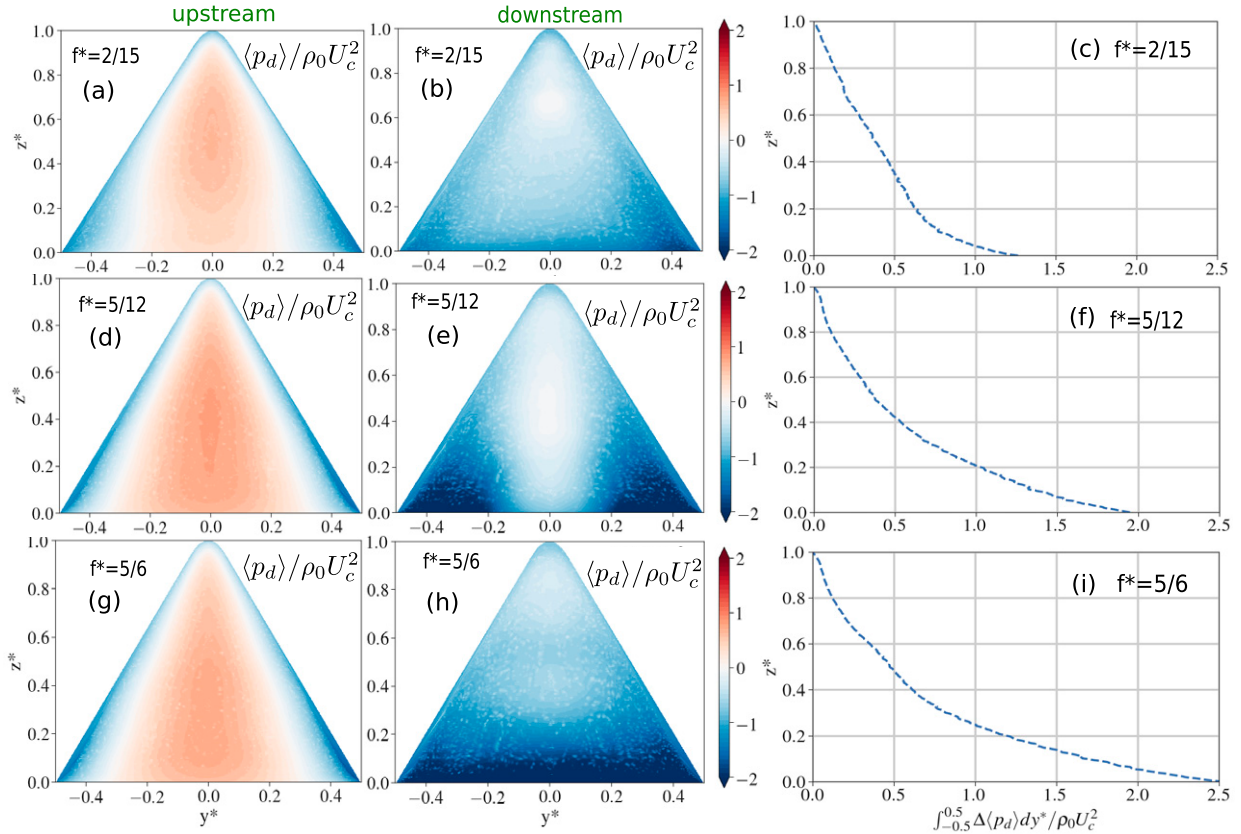
FIG. 3. Distribution of mean pressure ($\langle p_d \rangle / \rho_0 U_c^2$) on the upstream and downstream faces of the topography: (a),(b) $f^* = 2/15$; (d),(e) $f^* = 5/12$; and (g),(h) $f^* = 5/6$. The difference between upstream and downstream normalized pressure ($\langle p_d \rangle / \rho_0 U_c^2$) is integrated along $y^*$ and plotted in the last column for each case: (c) $f^* = 2/15$, (f) $f^* = 5/12$, and (i) $f^* = 5/6$.

pressure heightens the pressure anomaly between the fore and lee. As the barotropic flow decelerates between $T_2$ and $T_3$, the upstream pressure recedes concomitantly while the low pressure in the lee is sustained at $t = T_3$ (Fig. 4k). The lee eddy remains attached at this instant preserving the low pressure zone. The low pressure region continues to exist at the downstream face between $y^* = 0$ and 0.5 at $T_4$ (Fig. 4l). With the formation of persistent anticyclonic and cyclonic vortices on opposite sides during successive tidal cycles, the low pressure in the lee is maintained, albeit subject to lateral oscillations (see Pressure_JPO_fstar_5_6.mov in the online supplemental material). The outcome is an elevated mean drag.

For case $f^* = 5/12$, the pressure drop downstream of the obstacle is symmetric owing to the nature of the vortex shedding for this case. The low pressure region begins to form immediately after the lateral separation of the eddies at $t = T_1$ on both sides of the obstacle lee (Fig. 4f). While the barotropic current remains above its mean value $U_c$ between $t = T_1$ and $T_3$, the vortices continue to grow larger on either side of the hill (elaborated further in section 6 and Fig. 8). The pressure drop across the hill increases concurrently in Figs. 4f and 4g. At the zero velocity phase ($t = T_4$), the recirculating fluid at low pressure accelerates upstream relative to the

barotropic flow. A region of positive dynamic pressure (Fig. 4h) is identified at this instant near $x^* = 0.5$ and $y^* = 0$, while the pressure upstream at the obstacle center plane ($x^* = -0.5$ and $y^* = 0$) drops below zero momentarily. The eddy-induced low pressure zone remains attached at $x^*$, $y^* = (0.5, \pm0.5)$. This configuration is reset to Fig. 4e as the background flow gains momentum in the next cycle.

The instantaneous dynamic pressure $p_d$ has contributions from two sources: the added mass and flow separation [see Eq. (6)]. When the tidal frequency is larger, the added mass component increases owing to its dependence on the tidal acceleration magnitude $U_t \Omega_t$. This is likely to occur when $f^* = 2/15$ as corroborated by normalized $p_d$ in Figs. 4a–d. At $T_1$, the tidal acceleration reaches its maximum value and the dynamic pressure $p_d/\rho_0 U_c^2$ drops below $-2.5$ over a large region in the obstacle lee (Fig. 4a). Similarly, at the phase of maximum tidal deceleration ($t = T_3$), $p_d/\rho_0 U_c^2$ exceeds 2.5 over a large region upstream of the obstacle (Fig. 4c). At instances of zero acceleration ($t = T_2$ and $T_4$), the dynamic pressure is purely associated with flow separation. At $T_2$, the low pressure region in the lee (Fig. 4b) is generated due to the attached eddy in Fig. 2c, while the high $p_d$ upstream is generated by the impinging current. On the contrary, at $T_4$, the pressure anomalies in the obstacle center plane are
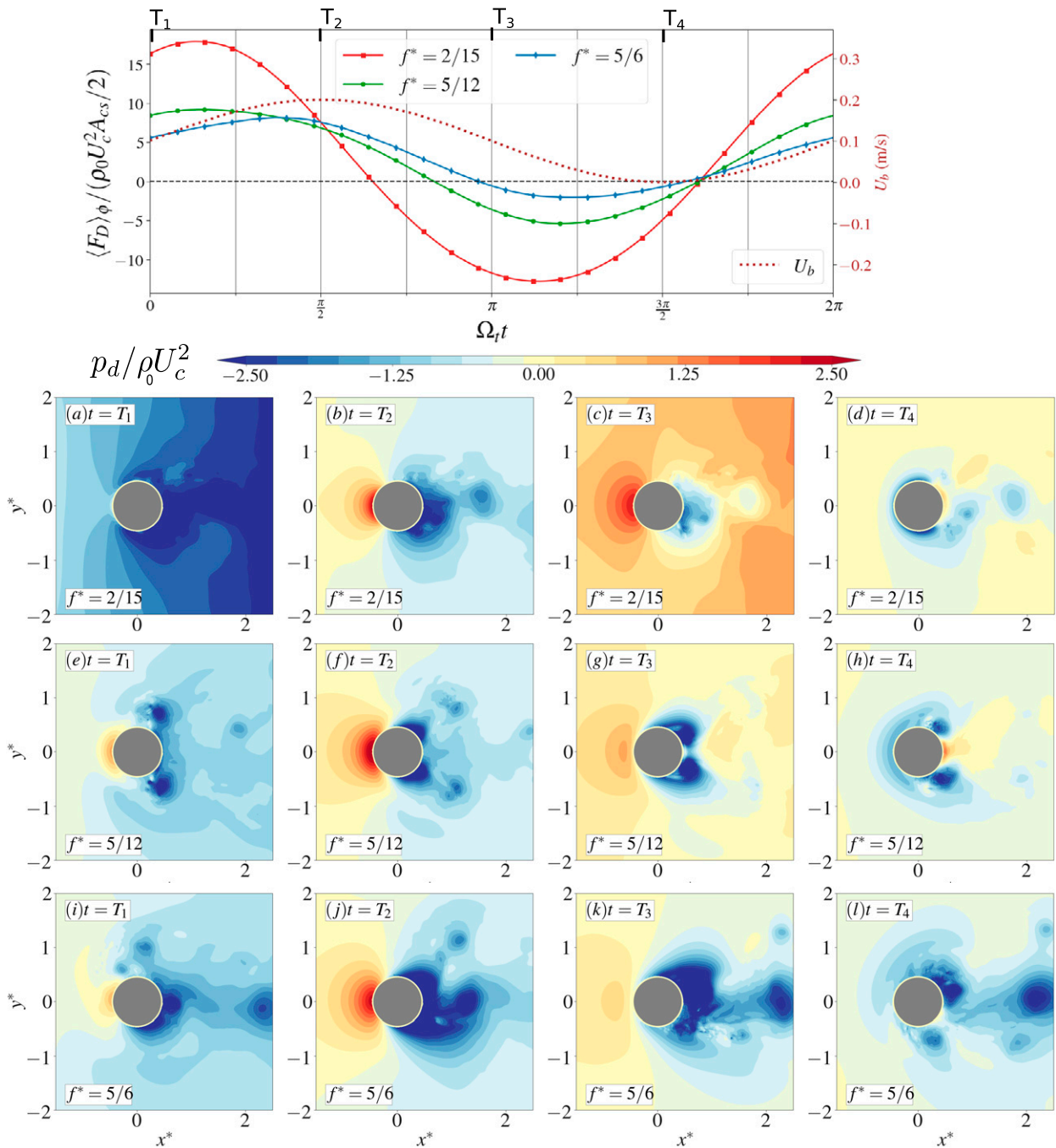
FIG. 4. (top) Variation of normalized phase-averaged drag force ($\langle F_D \rangle_\phi$) with tidal phase $\Omega_t t$, plotted for $f^* = 2/15, 5/12,$ and $5/6$ cases. The barotropic velocity $U_b$ is represented by the dotted line in the top panel. (bottom) The instantaneous contours of dynamic pressure $p_d$ are shown at four phases $T_1$, $T_2$, $T_3$, and $T_4$ (marked in the top panel) for cases (a)–(d) $f^* = 2/15$, (e)–(h) $f^* = 5/12$, and (i)–(l) $f^* = 5/6$ at $z^* = 0.02$. The projection of obstacle area in the streamwise direction is denoted as $A_{cs}$.

marginal (Fig. 4d). At the lateral sides of the obstacle, a weak pressure drop is observed, attributed to the vortex pulses discussed earlier. The tidal period is smaller than the natural eddy shedding time scale by a factor of 7.5 for this case. This constrains the size of the attached eddy to a small

vortex pulse, which has a correspondingly weak effect on the pressure drop.

The temporal variability of $p_d$ directly affects the variation in form drag as illustrated by the phase-averaged form drag $\langle F_D \rangle_\phi$ in the header of Fig. 4. The form drag exhibits large
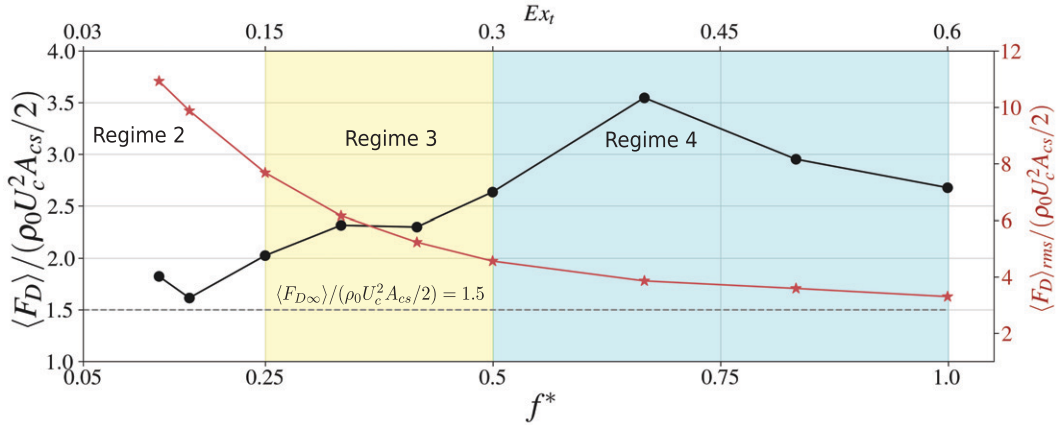
FIG. 5. Variation of mean drag force ($\langle F_D \rangle$) and its root-mean-square value ($\langle F_D \rangle_{\mathrm{rms}}$) with $f^*$. The gray dashed line denotes the normalized mean drag in the $f^* = \infty$ (no-tide) case (represented as $\langle F_{D\infty} \rangle$).

modulation in the $f^* = 2/15$ case. Also, the phase difference between $\langle F_D \rangle_\phi$ and $U_b$ exceeds $\pi/4$. Recall that the inertial drag has a phase difference of $\pi/2$ with $U_b$. Therefore, it is possible that instantaneous inertial drag contributions are important in this case. To confirm this, we follow the procedure of Warner and MacCready (2009) to estimate the ratio of inertial drag to separation drag for our obstacle geometry. We assume that the magnitude of $F_D^S$ is equal to the bluff-body drag estimate of $\rho_0 A_{cs} U_c^2 / 2$ and that $C_a = 1$ in Eq. (7) [for explanation, see Warner and MacCready (2009, p. 2979)]. For the conical obstacle, and taking $R = U_t/U_c = 1$,

$$\frac{|F_D^I|}{|F_D^S|} = \frac{2\pi}{3\mathrm{Ex}_t} \approx \frac{3.5}{f^*}, \tag{10}$$

where the second equality follows from $f^* = 1.66\mathrm{Ex}_t$ from section 1. As $f^*$ increases, the inertial component of form drag decreases. Separation drag becomes more prominent relative to inertial drag. This makes sense because at larger $f^* = f_{s,c}/f_t$, the tidal acceleration is weaker which causes the magnitude of inertial drag to decrease. Thus the phase difference between $\langle F_D \rangle_\phi$ and $U_b$ is smaller than $\pi/2$ at $f^* = 5/12$ and $5/6$.

### b. States of high drag

From the preceding text, it is clear that the pressure anomalies on the obstacle change significantly owing to tidal oscillations. Here we demonstrate that tidal oscillations lead to high levels of instantaneous and mean drag. The ratio of inertial drag to separation drag is inversely related to $f^*$ as shown in Eq. (10). It varies from a value of approximately 4 at $f^* = 5/6$ to 25 at $f^* = 2/15$. Clearly the contribution of inertial drag exceeds the separation drag within the tidal cycle, especially for low $f^*$ cases. Figure 4 showed that normalized $\langle F_D \rangle_\phi$ at $f^* = 2/15$ reached values of up to 16 during the tidal cycle just after $t = T_1$ and dropped rapidly below $-10$ near $T_3$. On the other hand, $\langle F_D \rangle_\phi$ has a smaller variance over the tidal cycle in the cases with $f^* = 5/12$ and $5/6$. In these two cases, large-eddy cores in the lee generate zones of low pressure with high

magnitude which remain at the obstacle periphery throughout the tidal cycle (Figs. 4e–l). The longer residence time of the attached low pressure zone enhances the separation drag $F_D^S$. The deviation of $\langle F_D \rangle_\phi$ from its cycle-averaged mean value is also much smaller. The values of $\langle F_D \rangle_\phi$ lie between $-5$ and 8 for this case.

Quantifying the mean and RMS values of $F_D$ is key in this comparative analysis. The time averaged value, namely $\langle F_D \rangle$, offers a diagnosis of high-drag states by nearly eliminating the contribution from inertial drag and providing an estimate of the separation drag $F_D^S$. Parameterization of separation drag is important owing to its ability to extract momentum from the flow. To this end, the normalized $\langle F_D \rangle$ and $\langle F_D \rangle_{\mathrm{rms}}$ are plotted in Fig. 5 as a function of $f^*$. The normalized form drag or the drag coefficient is $\langle F_D \rangle/(\rho_0 U_c^2 A_{cs}/2)$, where $A_{cs}$ is the projected obstacle area in the streamwise direction. The value of form drag coefficient in the $f^* = \infty$ case is 1.5. In the tidally modulated cases, the mean form drag coefficient generally increases with increasing $f^*$. The larger size and longer residence time of the attached wake eddy contribute to the intensification of the pressure drop and its sustenance near the foot of the abyssal hill (Figs. 3h,i). As a result, a large increase in $\langle F_D \rangle$ (relative to $\langle F_{D\infty} \rangle$) is observed in regimes 3 and 4. The mean drag coefficient exceeds 3.5 in regime 4, and its average value over the cases of regime 4 is 3, signifying a twofold increase in form drag with respect to the steady case. In regime 3, there is a 60% increase in average form drag relative to $\langle F_{D\infty} \rangle$. In comparison, only a marginal increase of $\langle F_D \rangle$ is seen in regime 2. On the other hand, the RMS drag, $\langle F_D \rangle_{\mathrm{rms}}$, is strongly influenced by inertial forces. The RMS drag decays rapidly as $f^*$ increases, from a large value of 11 at $f^* = 2/15$ to 3.2 at $f^* = 1$. This monotonic decay is attributed to a reduction in the inertial drag associated with the tidal acceleration.

### c. Energy loss to form drag

Figure 6 shows the variation of the tidally averaged power loss $\langle F_D U_b \rangle$ normalized by $\rho_0 U_c^3 A_{cs}/2$ as a function of $f^*$. It is noteworthy that normalized $\langle F_D U_b \rangle$ is close to 5 across the
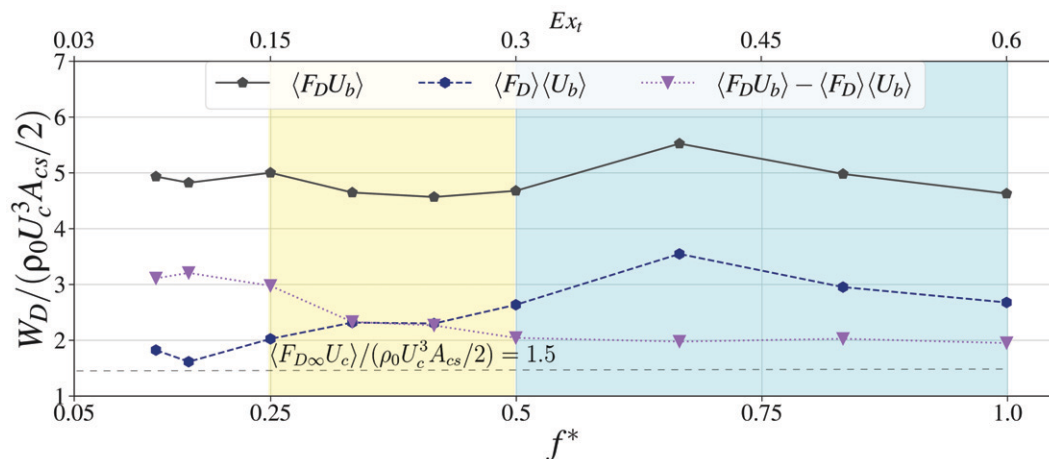
FIG. 6. Variation of rate of work done by drag ($W_D$) normalized by $\rho_0 U_c^3 A_{cs}/2$, with $f^*$. The black solid line represents normalized $\langle F_D U_b \rangle$ and the blue dashed line represents normalized $\langle F_D \rangle \langle U_b \rangle = \langle F_D \rangle U_c$. The difference between these two quantities is represented by the dotted purple line. The gray dashed line denotes the rate of work done in the $f^* = \infty$ (no-tide) case.

tidally modulated cases and the deviations from this magnitude are minimal. This value is at least 3 times larger than the value of 1.5 computed for $f^* = \infty$ case. This threefold increase is slightly larger than the factor of 2.5 increase expected from including the tidal velocity in the normalization factor (using $\langle U_b^3 \rangle$ instead of $U_c^3$) for the tidally modulated ($R = 1$) cases. The energy loss driven by the time-averaged form drag $\langle F_D \rangle \langle U_b \rangle = \langle F_D \rangle U_c$ follows a similar variability depicted by $\langle F_D \rangle$ in Fig. 5. This quantity is smaller than the mean tidal energy loss $\langle F_D U_b \rangle$ and the difference stems from the energy loss associated with the oscillatory part of form drag that is in phase with the tidal modulation. This difference is larger when $f^* \leq 0.25$. Therefore, interactions between the oscillatory part of form drag and tidal component of the flow are crucial in this regime and should be accounted for while calculating the total rate of kinetic energy loss.

### d. Frictional drag versus form drag

To ascertain the magnitude of form drag relative to the drag associated with the frictional bottom boundary layer (BBL), consider regime 4. The mean form drag $\langle F_{D\infty} \rangle = 3\rho_0 U_c^2 A_{cs}/2$. Assuming a coefficient of bottom friction ($C_f$) of approximately 0.002 based on previous studies (e.g., McCabe et al. 2006), the mean frictional drag ($\langle F^{BBL} \rangle$) is of the order $C_f \rho_0 U_c^2 A_b/2$, where $A_b$ is the projected area of the hill on the horizontal plane. Therefore, the ratio of mean form drag to frictional drag is

$$\frac{\langle F_{D\infty} \rangle}{\langle F^{BBL} \rangle} = \frac{3 A_{cs}}{C_f A_b} \approx 300. \tag{11}$$

Therefore, it is important to account for the form drag of 3D underwater obstacles when parameterizing bottom drag, especially when tidal oscillations are present. The interplay between form drag and spatiotemporal organization of the lee

eddies deserves attention. To this end, vortex dynamics are explored in the next section.

### 6. Vortex dynamics

Investigations of cylinder wakes created by homogeneous nonrotating flow, have often been used to add to our understanding of vortex dynamics in oceanic wakes (Chang et al. 2019). However, density stratification and planetary rotation influence the wake significantly. For example, Lin and Pao (1979) presented a detailed review of internal wave radiation and the emergence of thin lee vortices when $Fr_c < 1$. With the addition of rotation, Dong et al. (2006) showed manifestations of barotropic, baroclinic and centrifugal instabilities in the wake. The recent study of Puthan et al. (2021) showed that vortices in the far wake occur at frequencies coinciding with tidal subharmonics. Form drag is directly related to flow separation and near wake vortices. We discuss these facets and also the vertical organization of lee vortices in this section.

### a. Vertical structure of lee vortices

Figures 7a and 7c show contours of $\omega_z$ on horizontal planes at four different heights in the wake for $f^* = 5/12$ (regime 3) and 5/6 (regime 4). Velocity spectra at spatial probes chosen at these vertical heights are shown in Figs. 7b and 7d. Let $z_{div}^* \approx 1 - (U_c + U_t)/Nh = 0.7$ be an approximate estimate of the dividing vertical height (Sheppard 1956; Drazin 1961), below which the fluid is driven laterally around the obstacle. The four vertical heights in Fig. 7 are chosen such that $z^* < z_{div}^*$.

For $f^* = 5/12$ (Fig. 7a), laterally symmetric dipoles, attached to the obstacle, form along its vertical extent. Farther in the wake beyond $x^* = 2$, discrete eddies remain scattered and disorganized. At this stage, these eddies do not exhibit the spatial configuration of a Kármán vortex street.

For the case of $f^* = 5/6$ (Fig. 7c), the coherent vortices are larger and their shedding is asymmetrical. A region of both
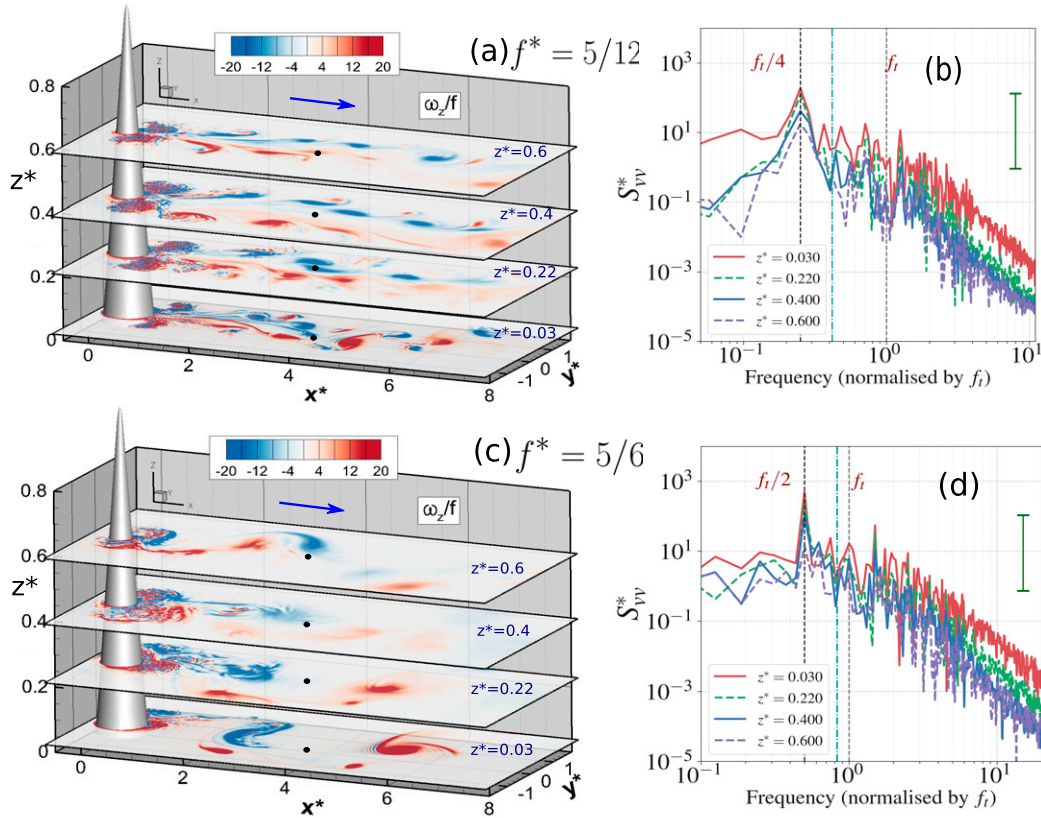
FIG. 7. Eddy formation is depicted by the normalized vertical vorticity ($\omega_z/f$) in four horizontal ($x$–$y$) planes: (a) $f^* = 5/12$ and (c) $f^* = 5/6$. (b),(d) Spectra of spanwise velocity $S_{vv}^* = S_{vv}/U_c^2$, plotted at four probes [black dots in (a) and (c), respectively] chosen at different vertical heights located at $x^* = 4$ and $y^* = 0$. The green bar in (b) and (d) shows the 95% confidence interval of the spectrum.

negative and positive vorticity remains attached to the topography along its vertical extent. Beyond $x^* = 1$, a large cyclonic (positive) vortex is followed by a large anticyclonic (negative) vortex at $z^* = 0.03$ and 0.22. These two vortices are found to be aligned vertically up to a height of $O(U_t/N)$. Similar aligned vortices were also observed in the $f^* = 5/12$ case, albeit smaller in diameter and more scattered. A possible explanation may stem from the vortex separation being initiated by the tidal forcing. To illustrate this, the spectra of spanwise velocity ($S_{vv}^*$) are plotted at different vertical heights for $f^* = 5/12$ and $f^* = 5/6$ cases in Figs. 7b and 7d. The frequency of lateral oscillations from $S_{vv}^*$ is used to ascertain the vortex shedding frequency. Vortices are shed at the same instant during the tidal cycle along the vertical extent of the obstacle (not shown). In addition, in the far wake at $z^* < z_{div}^*$, the vortices are observed at a uniform frequency of $f_t/4$ in $f^* = 5/12$ case and $f_t/2$ in $f^* = 5/6$ case. The timing of the flow separation may help align the vortices along the $z$ direction up to a vertical length scale permitted by the background stratification. At elevations above $z_{div}^*$, the transient lee waves interfere strongly with the coherent structures in the wake (see Puthan et al. 2020). Near-wake turbulence creates small-scale patches of vorticity in both cases, up to two diameters

away from the obstacle. However, we emphasize that their instantaneous presentation is qualitatively different from a classical Kármán vortex street over the vertical extent of the hill.

### b. Symmetric eddy dipoles

The symmetric twin dipoles shown previously in Fig. 2e are created through a sequence of events presented in Fig. 8. A locally adverse streamwise pressure gradient (shown in Figs. 4e,f) develops on either lateral side of the obstacle. While the barotropic flow remains positive, as in Fig. 8a, two opposite-signed vortices form in the recirculation zone and grow in size until the velocity approaches zero. As the tide-associated pressure gradient changes sign at the zero velocity phase, the high vorticity fluid accelerates upstream relative to the background flow on both lateral sides. During this event, additional vorticity of opposite sign is generated from shear when this fluid is near the obstacle. For example, the attached anticyclonic eddy in Fig. 8a accrues positive vorticity in Fig. 8b during its deflection to the $+y$ direction. Thus, twin dipoles form symmetrically on either lateral side of the obstacle. During the subsequent acceleration phase, the dipoles gain enough momentum to advect downstream (Fig. 8c).
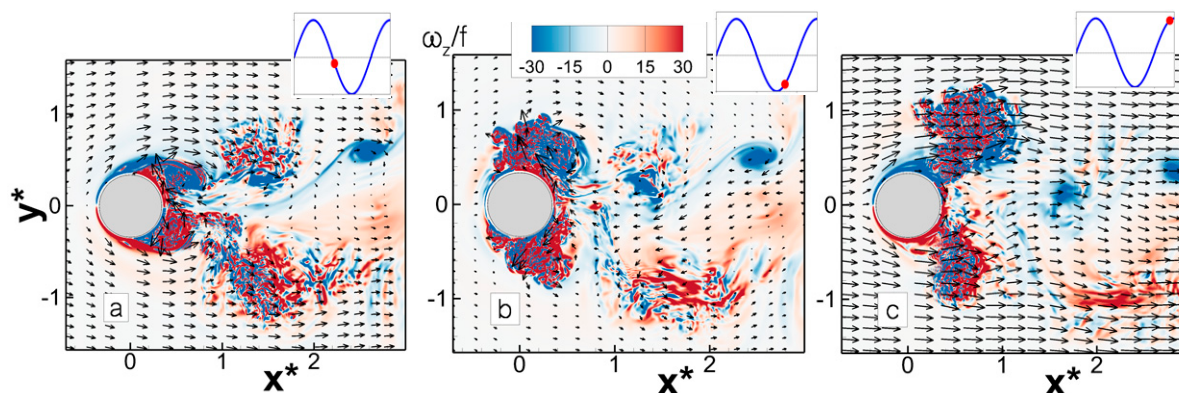
FIG. 8. Normalized vertical vorticity ($\omega_z/f$) at three different phases of a tidally perturbed wake at $f^* = 5/12$: (a) $t/T = 18.52$, (b)$t/T = 18.85$, and (c) $t/T = 19.19$.

At the same instant, a new vortex pair starts to grow near the separation points, completing a full cycle of oscillation.

The formation of the symmetric vortices is phase locked to the tidal cycle. Note that the positive vorticity generated by the upstream flow (directed to the $+y$ direction) in the previous tidal cycle (located at $x^*, y^* = 1.5, 0.5$) in Fig. 8a, decays in the present tidal cycle, as shown in Figs. 8b and 8c. The vortices also lose their lateral symmetry beyond $x^* = 1.5$. Tidal forcing aids in the symmetrical placement of vortices up to an excursion distance of $U_t/f_t$, or equivalently, $x^* = 1.57$ for this case. Beyond $x^* = 1.57$, a staggered and distorted pattern of vortices occurs (see Fig. 2e). Deviation of the wake vortex frequency $f_s$ from the tidal frequency $f_t$ occurs in this region, as elaborated in the next section.

### c. Temporal variation of vorticity

Hovmöller diagrams of normalized vorticity in Fig. 9 demonstrate clearly that transitions of the vortex frequency from the near to the far wake vary among regimes 2–4. Space–time ($y$–$t$) contours of vertical vorticity are plotted at two stations: S1 in the near wake and S2 in the far wake (see dashed lines in Figs. 2c,e,g). In Fig. 9a, the signature of the tidal frequency is observed in the vortex pulses spaced over one tidal period ($T$) for $f^* = 2/15$. These pulses are arranged in the form of a slowly varying large-scale sinuous (antisymmetric) mode. The sinuous mode evolves into a row of opposite-signed vortices at S2 (Fig. 9b). The signature of the individual vortex pulses disappears at S2 leaving large-scale coherent vortices separated by the time period $T_s$. The vortex period ($T_s$) in the far wake aligns with the natural shedding period of the obstacle wake, $T_{s,c}$.

Case $f^* = 5/12$ exhibits a laterally symmetric vortex pattern at S1, depicted in Fig. 9c. These vortex structures repeat every tidal cycle. The unstable symmetric mode transitions into an antisymmetric downstream wake made up of coherent vortices in Fig. 9d. These vortices are separated by $T_s = 4T$, demonstrating the tidal synchronization noted in Puthan et al. (2021). Thus the wake vortex frequency is modified to $f_t/4$. In other words, during every tidal cycle the symmetric vortices

feed their vorticity into a larger vortex downstream, formed every four tidal cycles.

In the $f^* = 5/6$ case, the wake is strongly asymmetric in the lateral direction at S1 (Fig. 9e). Large vortex lobes repeat once every two cycles and extend laterally. The lateral extent stretches farther at S2 relative to the previous two cases, as seen in Fig. 9f. The wake width is as large as $4.5D$ (extending from $y^* \approx -2.5$ to $y^* \approx 2$), compared to $3D$ and $2.2D$ for $f^* = 5/12$ and $2/15$. A temporally distorted wake is observed at S2 in the $f^* = 5/6$ case, wherein the larger patches of negative vorticity are observed near the center while smaller vortices of same sign are laterally offset by approximately $2D$ from the center plane. The space–time plot reveals thin filaments of positive vorticity in the temporal frame, in the far wake of $f^* = 5/12$ and $5/6$ cases. The far wake eddy frequency coincides with $f_t/2$ for $f^* = 5/6$.

To explore the time evolution of eddy vorticity injected into the wake, the absolute value of $\omega_z$ is volume averaged over a domain encompassing the hill and extending to a distance of $8D$ into the wake. Figure 10a shows the temporal evolution of normalized volume-averaged vorticity $\langle|\omega_z|\rangle_V/f$. The dotted line shows the variation in the barotropic velocity. For the $f^* = 2/15$ case, $\langle|\omega_z|\rangle_V$ varies in phase with $U_b$. The pulses of vorticity which form during the maximum velocity phase of every tidal cycle are likely responsible for the small increases of $\langle|\omega_z|\rangle_V$ from its mean value. At $f^* = 5/12$, $\langle|\omega_z|\rangle_V$ increases at the low-velocity phase during every tidal cycle. During the shedding of symmetric vortices, the low-velocity phase is accompanied by additional vorticity from shear layer roll-up at the obstacle (Fig. 8). The result is an increase of $\langle|\omega_z|\rangle_V$ near the zero-velocity phase. On the other hand, larger variations from the mean occur in $\langle|\omega_z|\rangle_V$ values when $f^* = 5/6$.

Time averages of $\langle|\omega_z|\rangle_V/f$ are plotted over a range of $f^*$ values in Fig. 10b. Net vorticity added by the tides is not significant when $f^*$ lies below 0.2 (Fig. 10b). Above this threshold, a gradual increase is noticed in $\langle|\omega_z|\rangle_{Vt}$ until it reaches a value of 4 at $f^* = 5/12$ and does not increase appreciably beyond that. This may be explained as follows. Over a tidal cycle, high vorticity fluid in the obstacle vicinity is advected by
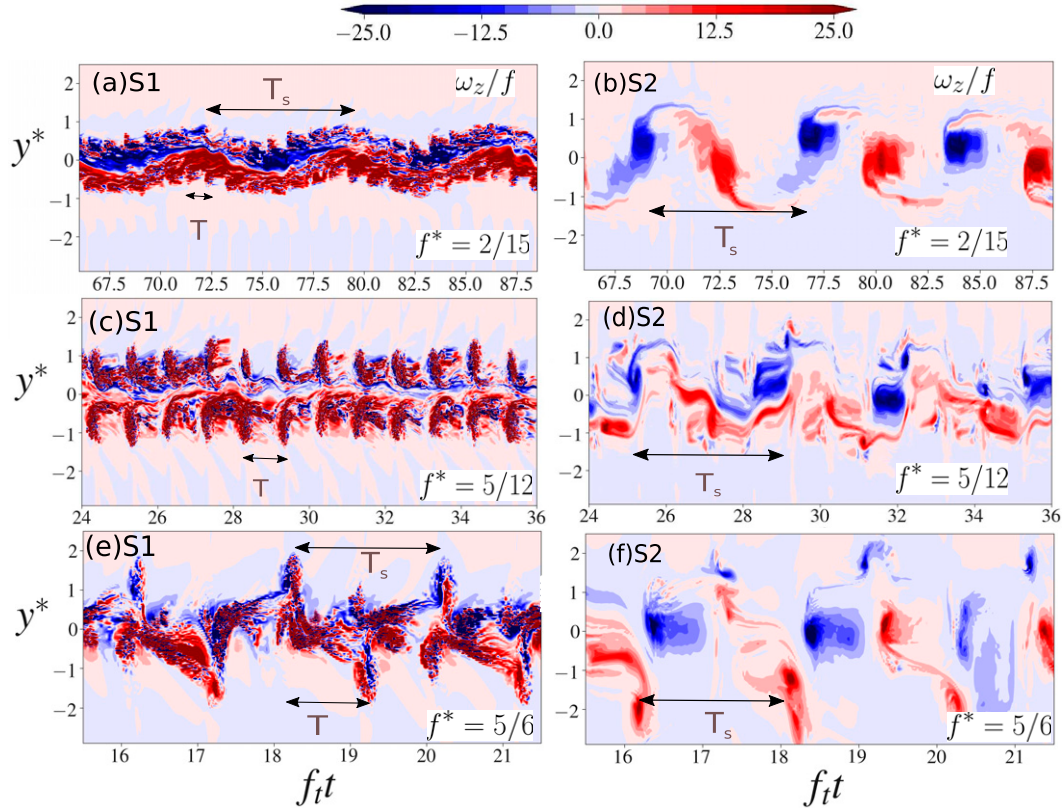
FIG. 9. Time evolution of vertical vorticity ($\omega_z/f$) is depicted by a $y$–$t$ Hovmöller diagram, at stations S1 (at $x^*$, $z^* = 1, 0.25$) and S2 (at $x^*$, $z^* = 4, 0.25$) for three cases: (a),(b) $f^* = 2/15$; (c),(d) $f^* = 5/12$; and (e),(f) $f^* = 5/6$. Here, $T$ is the tidal period and $T_s$ is the time period of far wake vortices. Note that the range of $f_t t$ decreases from the top to the bottom row. The stations S1 and S2 are indicated by brown dashed lines in Fig. 2.

a distance of $U_c T$. This fluid migrates into the wake permanently if $U_c T$ exceeds $\mathcal{O}(D)$. In other words, the tidal flow adds vorticity to the wake when $U_c T/D > \mathcal{O}(1)$. Simplifying using the relation $f^* = 1.66 \mathrm{Ex}_t$ (from section 1) this condition is equivalent to $f^* > \mathcal{O}(0.25)$. At larger $f^* = f_{s,c}/f_t$, the vortices have sufficient time to separate from the obstacle before the deceleration of barotropic current.

## 7. Discussion and conclusions

LES were undertaken to examine the wake created by a stratified tidally modulated flow ($U_b$) in the presence of weak background rotation. The barotropic flow $U_b$ has a mean component $U_c$, and a tidal component $U_t$ of equal strength. Since the Froude number $\mathrm{Fr}_c$ is small, the near-bottom flow is forced to separate laterally from the obstacle. As a result, large coherent eddies such as those observed in the ocean (e.g., Pawlak et al. 2003; MacKinnon et al. 2019), form in the lee. We find that the flow exhibits four regimes, based on vortex patterns, as summarized in Table 1. In the first regime where tides are absent, lee vortices separate from the obstacle at a constant frequency $f_{s,c}$ and form a Kármán vortex street downstream. In the next three regimes, the arrangement of vortices is altered by the tidal flow. Changes in flow

separation, accompanied by bottom-intensified pressure differences on the obstacle, are responsible for states of high drag in the tidally modulated cases, especially regime 4.

The effect of tidal oscillations is characterized by varying the relative frequency parameter ($f^* = f_{s,c}/f_t$) from $1/10$ to $1$. Three of the nine cases are chosen, namely, $f^* = 2/15, 5/12,$ and $5/6$ from regimes 2, 3, and 4, respectively, to illustrate the results. At $f^* = 2/15$ (regime 2), vortex pulses which occur every tidal cycle, feed vorticity into a larger eddy in the recirculation zone. These larger eddies form a Kármán vortex wake downstream. At $f^* = 5/12$ (regime 3), laterally symmetric eddy dipoles are shed in the near wake. The lateral symmetry is controlled by the tidal flow up to a streamwise distance of $U_t/f_t$. Beyond this location, the vortices partially break down or merge to create a disorganized wake downstream. This event is accompanied by a change in the wake vortex frequency from $f_t$ to $f_t/4$. At $f^* = 5/6$ (regime 4), strong asymmetric shedding at a frequency of $f_t/2$ is observed in the entire wake. The wake is laterally wider in comparison to the other regimes.

The timing of the shed vortices is strongly influenced by the barotropic tidal oscillation. When $|\omega_z|$ is volume averaged over the wake, its temporal variation is affected by the tidal oscillation. At $f^* = 2/15$, the temporal evolution is in phase
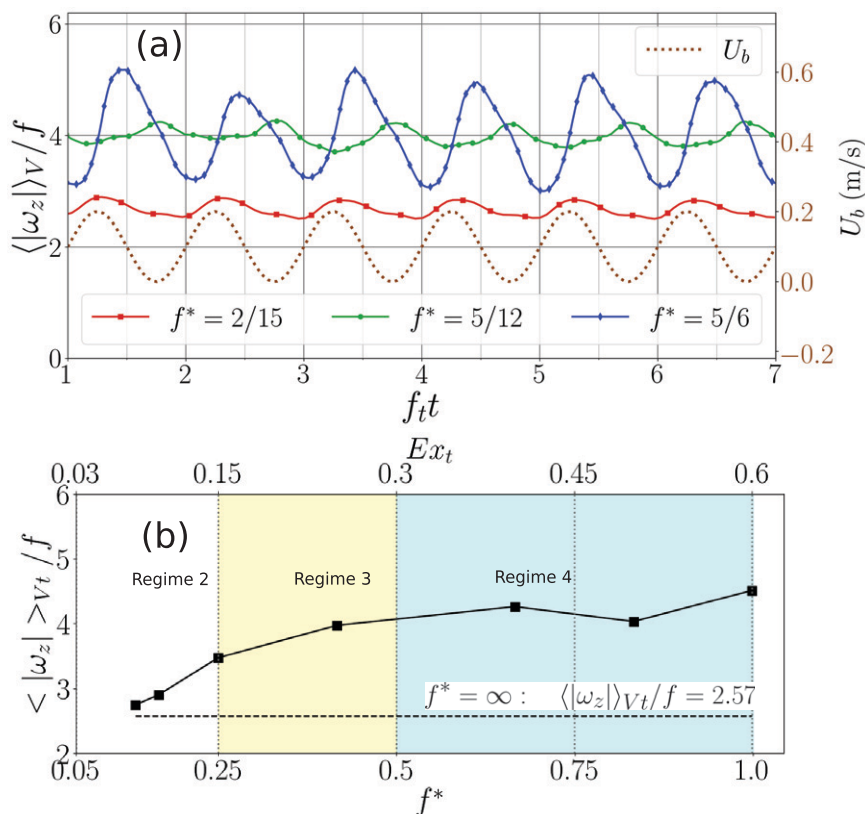
FIG. 10. (a) Volume-averaged vertical vorticity $\langle|\omega_z|\rangle_V = \int_0^V |\omega_z| dV/V$ plotted as a function of time for $f^* = 2/15, 5/12,$ and $5/6$ cases. (b) Variation of time averaged $\langle|\omega_z|\rangle_V$ shown as a function of $f^*$.

with tides owing to the formation of vortex pulses. On the other hand, at $f^* = 5/12$, the temporal evolution is out of phase with the tidal oscillation. Excess vorticity is added to the wake from the lateral motion of recirculating fluid and the attendant shear-layer roll-up during the low-velocity phase.

Changes in flow separation also lead to variations in pressure along the streamwise direction of the obstacle. The difference between the mean pressure field fore and aft of the hill ($\Delta\langle p_d\rangle$) is bottom intensified in cases $f^* = 5/12$ and $5/6$. At $f^* = 5/12$, the intensification is laterally offset from the centerline due to the impinging of the recirculating fluid on the obstacle centerline near the zero-velocity phase.

The normalized form drag, i.e., drag coefficient, obtained by integrating the pressure field over the obstacle surface area, varies among these cases. Form drag has two components, namely, the inertial and the separation drag. The separation drag is the dissipative part of form drag. The mean drag (averaged over several cycles) which is associated with the separation drag (Sarpkaya 2004; Warner and MacCready 2009), generally increases with increasing $f^*$. The bottom intensified values of $\Delta\langle p_d\rangle$ (associated with large eddies) and the longer eddy residence time in the lee contribute to approximately a twofold increase of mean drag coefficient in regime 4 relative to its value in the no-tide case. High drag states are also present in regime 3, wherein approximately a

60% increase is observed in mean drag coefficient relative to the no-tide case. Therefore, for a continuous distribution of topographic scales in the abyssal ocean, obstacles with $1/4 \le f^* \le 1$ can preferentially remove momentum from the background tidally modulated flow. The drag coefficient can be expected to be dependent on the obstacle shape. Therefore, the form drag amplification factor can also vary with the shape and aspect ratio of the topography, owing to changes in flow separation. The inertial drag force (associated with the magnitude of tidal acceleration) is dominant in regime 2, causing large variance of form drag within the tidal cycle in the $f^* = 2/15$ case. Since the inertial component of drag decreases with increasing $f^*$, so does the RMS drag. The rapidly varying pressure gradient associated with tidal forcing for $f^* = 2/15$ restricts the size of the lee eddy to $O(U_t/f_t)$ and diminishes the pressure anomalies during the zero-velocity phase of the tidal cycle. This leads to lower mean form drag. The tidal energy loss rate $\langle F_D U_b \rangle$ does not vary significantly on changing $f^*$. Although the work done by the mean form drag is higher in regimes 3 and 4, the large RMS drag in regime 2 interacts with the oscillatory component of the barotropic flow to elevate the total energy loss rate.

Warner and MacCready (2009) investigated a coastal headland in a purely tidal flow and did not find a significant effect of the excursion number (equivalently $f^*$) on separation drag

beyond Ex$_t$ of 0.25. Deviations of the present findings (regarding excursion number effects) from their results may be attributed to a difference in geometry (submerged conical obstacle) or the presence of a mean current in this study. The drag coefficient associated with mean form drag normalized using the obstacle frontal area in regime 4 is 3. Converting this to a value based on the obstacle plan area, the drag coefficient takes a value of approximately 0.6, substantially larger than the drag coefficient associated with the frictional bottom boundary layer of $O(10^{-3})$ estimated in previous work (e.g., Dewey and Crawford 1988). Thus, form drag owing to wakes of steep obstacles dominates frictional drag in tidally modulated currents.

*Data availability statement.* The data used in this study is available in the repository https://doi.org/10.5281/zenodo.6506920.

## REFERENCES

Acarlar, M. S., and C. R. Smith, 1987: A study of hairpin vortices in a laminar boundary layer. Part 1. Hairpin vortices generated by a hemisphere protuberance. *J. Fluid Mech.*, **175**, 1–41, https://doi.org/10.1017/S0022112087000272.

Black, K., and S. Gay, 1987: Eddy formation in unsteady flows. *J. Geophys. Res.*, **92**, 9514–9522, https://doi.org/10.1029/JC092iC09p09514.

Callendar, W., J. M. Klymak, and M. G. G. Foreman, 2011: Tidal generation of large sub-mesoscale eddy dipoles. *Ocean Sci.*, **7**, 487–502, https://doi.org/10.5194/os-7-487-2011.

Chang, M., S. Jan, C. Liu, Y. Cheng, and V. Mehsah, 2019: Observations of island wakes at high Rossby numbers: Evolution of submesoscale vortices and free shear layers. *J. Phys. Oceanogr.*, **49**, 2997–3016, https://doi.org/10.1175/JPO-D-19-0035.1.

Clément, L., A. M. Thurnherr, and L. C. S. Laurent, 2017: Turbulent mixing in a deep fracture zone on the Mid-Atlantic Ridge. *J. Phys. Oceanogr.*, **47**, 1873–1896, https://doi.org/10.1175/JPO-D-16-0264.1.

Denniss, T., J. H. Middleton, and R. Manasseh, 1995: Recirculation in the lee of complicated headlands: A case study of Bass Point. *J. Geophys. Res.*, **100**, 16087–16101, https://doi.org/10.1029/95JC01279.

Dewey, R. K., and W. R. Crawford, 1988: Bottom stress estimates from vertical dissipation rate profiles on the continental shelf. *J. Phys. Oceanogr.*, **18**, 1167–1177, https://doi.org/10.1175/1520-0485(1988)018<1167:BSEFVD>2.0.CO;2.

Dietrich, D. E., M. J. Bowman, C. A. Lin, and A. Mestasnunez, 1996: Numerical studies of small island wakes in the ocean. *Geophys. Astrophys. Fluid Dyn.*, **83**, 195–231, https://doi.org/10.1080/03091929608208966.

Dong, C., J. C. McWilliams, and A. F. Shchepetkin, 2006: Island wakes in deep water. *J. Phys. Oceanogr.*, **37**, 962–981, https://doi.org/10.1175/JPO3047.1.

Drazin, P., 1961: On the steady flow of a fluid of variable density past an object. *Tellus*, **13**, 239–251, https://doi.org/10.3402/tellusa.v13i2.9451.

Edwards, K. A., P. MacCready, J. M. Moum, G. Pawlak, J. M. Klymak, and A. Perlin, 2004: Form drag and mixing due to tidal flow past a sharp point. *J. Phys. Oceanogr.*, **34**, 1297–1312, https://doi.org/10.1175/1520-0485(2004)034<1297:FDAMDT>2.0.CO;2.

Egbert, G. D., and R. D. Ray, 2000: Significant dissipation of tidal energy in the deep ocean inferred from satellite altimeter data. *Nature*, **405**, 775–778, https://doi.org/10.1038/35015531.

Epifanio, C. C., and D. R. Durran, 2001: Three-dimensional effects in high-drag-state flows over long ridges. *J. Atmos. Sci.*, **58**, 1051–1065, https://doi.org/10.1175/1520-0469(2001)058<1051:TDEIHD>2.0.CO;2.

——, and R. Rotunno, 2005: The dynamics of orographic wake formation in flows with upstream blocking. *J. Atmos. Sci.*, **62**, 3127–3150, https://doi.org/10.1175/JAS3523.1.

Garcia-Villalba, M., N. Li, W. Rodi, and M. Leschziner, 2009: Large eddy simulation of separated flow over a three-dimensional axisymmetric hill. *J. Fluid Mech.*, **627**, 55–96, https://doi.org/10.1017/S0022112008005661.

Girton, J., and Coauthors, 2019: Flow-topography interactions in the Samoan Passage. *Oceanography*, **32**, 184–193, https://doi.org/10.5670/oceanog.2019.424.

Horwitz, R. W., S. Taylor, Y. Lu, J. Paquin, D. Schillinger, and D. A. Greenberg, 2021: Rapid reduction of tidal amplitude due to form Drag in a narrow channel. *Cont. Shelf Res.*, **213**, 104299, https://doi.org/10.1016/j.csr.2020.104299.

Hunt, J., and W. Snyder, 1980: Experiments on stably and neutrally stratified flow over a model three-dimensional hill. *J. Fluid Mech.*, **96**, 671–704, https://doi.org/10.1017/S0022112080002303.

Jagannathan, A., K. Winters, and L. Armi, 2019: Stratified flows over and around long dynamically tall mountain ridges. *J. Atmos. Sci.*, **76**, 1265–1287, https://doi.org/10.1175/JAS-D-18-0145.1.

——, K. Srinivasan, J. C. McWilliams, M. J. Molemaker, and A. L. Stewart, 2021: Boundary-layer-mediated vorticity generation in currents over sloping bathymetry. *J. Phys. Oceanogr.*, **51**, 1757–1778, https://doi.org/10.1175/JPO-D-20-0253.1.

Keulegan, G. H., and L. H. Carpenter, 1958: Forces on cylinders and plates in an oscillating fluid. *Amer. Soc. Mech. Eng.*, **60**, 423–440, https://doi.org/10.6028/jres.060.043.

Klymak, J. M., 2018: Nonpropagating form Drag and turbulence due to stratified flow over large scale abyssal hill topography. *J. Phys. Oceanogr.*, **48**, 2383–2395, https://doi.org/10.1175/JPO-D-17-0225.1.

Lamb, H., 1930: *Hydrodynamics.* Cambridge University Press, 738 pp.

Ledwell, J. R., E. T. Montgomery, K. L. Polzin, L. C. S. Laurent, R. W. Schmitt, and J. M. Toole, 2000: Evidence for enhanced mixing over rough topography in the abyssal ocean. *Nature*, **403**, 179–182, https://doi.org/10.1038/35003164.

Lighthill, J., 1986: Fundamentals concerning wave loading on offshore structures. *J. Fluid Mech.*, **173**, 667–681, https://doi.org/10.1017/S0022112086001313.

Lin, J. T., and Y. H. Pao, 1979: Wakes in stratified fluids: A review. *Annu. Rev. Fluid Mech.*, **11**, 317–338, https://doi.org/10.1146/annurev.fl.11.010179.001533.

Liu, C., and M. Chang, 2018: Numerical studies of submesoscale island wakes in the Kuroshio. *J. Geophys. Res. Oceans*, **123**, 5669–5687, https://doi.org/10.1029/2017JC013501.

MacCready, P., and G. Pawlak, 2001: Stratified flow along a corrugated slope: Separation drag and wave drag. *J. Phys. Oceanogr.*,

**31**, 2824–2839, https://doi.org/10.1175/1520-0485(2001)031<2824:SFAACS>2.0.CO;2.

MacKinnon, J. A., M. H. Alford, G. Voet, K. Zeiden, T. M. S. Johnston, M. Siegelman, S. Merrifield, and M. Merrifield, 2019: Eddy wake generation from broadband currents near Palau. *J. Geophys. Res. Oceans*, **124**, 4891–4903, https://doi.org/10.1029/2019JC014945.

Magaldi, M. G., T. M. Ozgokmen, A. Griffa, E. P. Chassignet, M. Iskandarani, and H. Peters, 2008: Turbulent flow regimes behind a coastal cape in a stratified and rotating environment. *Ocean Modell.*, **25**, 65–82, https://doi.org/10.1016/j.ocemod.2008.06.006.

McCabe, R. M., P. MacCready, and G. Pawlak, 2006: Form Drag due to flow separation at a headland. *J. Phys. Oceanogr.*, **36**, 2136–2152, https://doi.org/10.1175/JPO2966.1.

Morison, J. R., J. W. Johnson, and S. A. Schaaf, 1950: The force exerted by surface waves on piles. *J. Pet. Tech.*, **2**, 149–154, https://doi.org/10.2118/950149-G.

Musgrave, R. C., J. A. Mackinnon, R. Pinkel, and A. F. Waterhouse, 2016: Tidally driven processes leading to near-field turbulence in a channel at the crest of the Mendocino Escarpment. *J. Phys. Oceanogr.*, **46**, 1137–1155, https://doi.org/10.1175/JPO-D-15-0021.1.

Nash, J. D., and J. N. Moum, 2001: Internal hydraulic flows on the continental shelf: High drag states over a small bank. *J. Geophys. Res.*, **106**, 4593–4611, https://doi.org/10.1029/1999JC000183.

Nikurashin, M., and R. Ferrari, 2010: Radiation and dissipation of internal waves generated by geostrophic flows impinging on small scale topography: Application to the Southern Ocean. *J. Phys. Oceanogr.*, **40**, 2025–2042, https://doi.org/10.1175/2010JPO4315.1.

——, and S. Legg, 2011: A mechanism for local dissipation of internal tides generated at rough topography. *J. Phys. Oceanogr.*, **41**, 378–395, https://doi.org/10.1175/2010JPO4522.1.

Pawlak, G., P. MacCready, K. A. Edwards, and R. McCabe, 2003: Observations on the evolution of tidal vorticity at a stratified deep water headland. *Geophys. Res. Lett.*, **30**, 2234, https://doi.org/10.1029/2003GL018092.

Perfect, B., N. Kumar, and J. Riley, 2018: Vortex structures in the wake of an idealized seamount in rotating, stratified flow. *Geophys. Res. Lett.*, **45**, 9098–9105, https://doi.org/10.1029/2018GL078703.

——, ——, and ——, 2020: Energetics of seamount wakes. Part 2: Wave fluxes. *J. Phys. Oceanogr.*, **50**, 1383–1398, https://doi.org/10.1175/JPO-D-19-0104.1.

Puthan, P., M. Jalali, J. L. Ortiz-Tarin, K. Chongsiripinyo, G. Pawlak, and S. Sarkar, 2020: The wake of a three-dimensional underwater obstacle: Effect of bottom boundary conditions. *Ocean Modell.*, **149**, 101611, https://doi.org/10.1016/j.ocemod.2020.101611.

——, S. Sarkar, and G. Pawlak, 2021: Tidal synchronization of lee vortices in geophysical wakes. *Geophys. Res. Lett.*, **48**, e2020GL090905, https://doi.org/10.1029/2020GL090905.

Rudnick, D. L., K. L. Zeiden, C. Y. Ou, T. M. S. Johnston, J. A. MacKinnon, M. H. Alford, and G. Voet, 2019: Understanding

vorticity caused by flow passing an island. *Oceanography*, **32**, 66–73, https://doi.org/10.5670/oceanog.2019.412.

Sarpkaya, T., 2001: On the force decompositions of Lighthill and Morrison. *J. Fluids Struct.*, **15**, 227–233, https://doi.org/10.1006/jfls.2000.0342.

——, 2004: A critical review of the intrinsic nature of vortex-induced vibrations. *J. Fluids Struct.*, **19**, 389–447, https://doi.org/10.1016/j.jfluidstructs.2004.02.005.

Sheppard, P. A., 1956: Airflow over mountains. *Quart. J. Roy. Meteor. Soc.*, **82**, 528–529, https://doi.org/10.1002/qj.49708235418.

Signell, R. P., and W. R. Geyer, 1991: Transient eddy formation around headland. *J. Geophys. Res.*, **96**, 2561–2575, https://doi.org/10.1029/90JC02029.

Srinivasan, K., J. C. McWilliams, J. Molemaker, and R. Barkan, 2018: Submesoscale vortical wakes in the lee of the topography. *J. Phys. Oceanogr.*, **49**, 1949–1971, https://doi.org/10.1175/JPO-D-18-0042.1.

——, ——, and A. Jagannathan, 2021: High vertical shear and dissipation in equatorial topographic wakes. *J. Phys. Oceanogr.*, **51**, 1985–2001, https://doi.org/10.1175/JPO-D-20-0119.1.

Voet, G., M. H. Alford, J. A. MacKinnon, and J. D. Nash, 2020: Eddy wake generation from broadband currents near Palau. *J. Phys. Oceanogr.*, **50**, 1489–1507, https://doi.org/10.1175/JPO-D-19-0257.1.

Vosper, S., I. Castro, W. Snyder, and S. Mobbs, 1999: Experimental studies of strongly stratified flow past three-dimensional orography. *J. Fluid Mech.*, **390**, 223–249, https://doi.org/10.1017/S0022112099005133.

Warner, S. J., and P. MacCready, 2009: Dissecting the pressure field in tidal flow past a headland: When is form drag "real"? *J. Phys. Oceanogr.*, **39**, 2971–2984, https://doi.org/10.1175/2009JPO4173.1.

——, and ——, 2014: The dynamics of pressure and form drag on a sloping headland: Internal waves versus eddies. *J. Geophys. Res. Oceans*, **119**, 1554–1571, https://doi.org/10.1002/2013JC009757.

——, ——, J. M. Moum, and J. D. Nash, 2012: Measurement of tidal form drag using seafloor pressure sensors. *J. Phys. Oceanogr.*, **43**, 1150–1172, https://doi.org/10.1175/JPO-D-12-0163.1.

Wijesekera, H. W., E. Jarosz, W. J. Teague, D. W. Wang, D. B. Fribance, J. M. Moum, and S. J. Warner, 2014: Measurements of form and frictional drags over a rough topographic bank. *J. Phys. Oceanogr.*, **44**, 2409–2432, https://doi.org/10.1175/JPO-D-13-0230.1.

Wright, C. J., R. B. Scott, P. Ailliot, and D. Furnival, 2014: Lee wave generation rates in the deep ocean. *Geophys. Res. Lett.*, **41**, 2434–2440, https://doi.org/10.1002/2013GL059087.

Yu, X., J. H. Rosman, and J. L. Hench, 2018: Interaction of waves with idealised high-relief bottom roughness. *J. Geophys. Res. Oceans*, **123**, 3038–3059, https://doi.org/10.1029/2017JC013515.

Zhang, X., and M. Nikurashin, 2020: Small scale topographic form stress and local dynamics of the Southern Ocean. *J. Geophys. Res. Oceans*, **125**, https://doi.org/10.1029/2019JC015420.